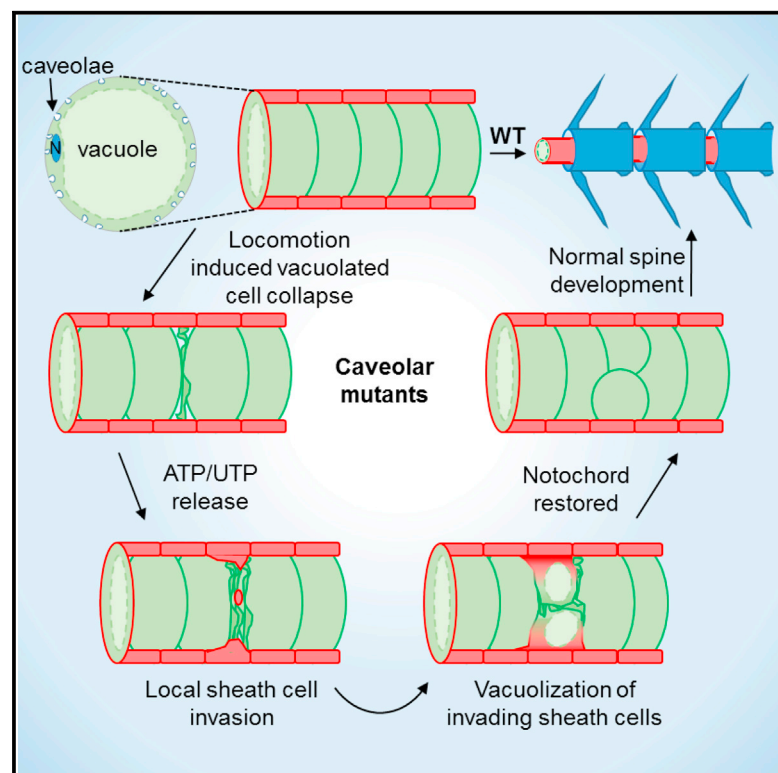


Current Biology

Sheath Cell Invasion and Trans-differentiation Repair Mechanical Damage Caused by Loss of Caveolae in the Zebrafish Notochord

Graphical Abstract



Authors

Jamie Garcia, Jennifer Bagwell, Brian Njaine, ..., Jason W. Locasale, Didier Y.R. Stainier, Michel Bagnat

Correspondence

m.bagnat@cellbio.duke.edu

In Brief

Garcia et al. show that plasma membrane caveolae play a mechano-protective role in vacuolated cells of the zebrafish notochord. Loss of caveolae causes vacuolated cell collapse during locomotion. Then, invasion of neighboring sheath cells and their trans-differentiation into vacuolated cells repair the damage, allowing normal spine development.

Highlights

- Caveolae are conserved cell-surface structures in notochord vacuolated cells
- Loss of caveolae causes motion-dependent vacuolated cell collapse in zebrafish
- Vacuolated cell collapse causes NTP release, sheath cell invasion, and vacuolization
- Differentiation of sheath cells restores the notochord and safeguards spine formation

Sheath Cell Invasion and Trans-differentiation Repair Mechanical Damage Caused by Loss of Caveolae in the Zebrafish Notochord

Jamie Garcia,^{1,5} Jennifer Bagwell,^{1,5} Brian Njaine,² James Norman,¹ Daniel S. Levic,¹ Susan Wopat,¹ Sara E. Miller,⁴ Xiaojing Liu,³ Jason W. Locasale,³ Didier Y.R. Stainier,² and Michel Bagnat^{1,6,*}

¹Department of Cell Biology, Duke University, Durham, NC 27710, USA

²Department of Developmental Genetics, Max Planck Institute for Heart and Lung Research, 61231 Bad Nauheim, Germany

³Department of Pharmacology and Cancer Biology, Duke University, Durham, NC 27710, USA

⁴Department of Pathology, Duke University, Durham, NC 27710, USA

⁵These authors contributed equally

⁶Lead Contact

*Correspondence: m.bagnat@cellbio.duke.edu

<http://dx.doi.org/10.1016/j.cub.2017.05.035>

SUMMARY

The notochord, a conserved axial structure required for embryonic axis elongation and spine development, consists of giant vacuolated cells surrounded by an epithelial sheath [1–3]. During morphogenesis, vacuolated cells maintain their structural integrity despite being under constant mechanical stress [4]. We hypothesized that the high density of caveolae present in vacuolated cells [5, 6] could buffer mechanical tension. Caveolae are 50- to 80-nm membrane invaginations lined by cage-like polygonal structures [7, 8] formed by caveolin 1 (Cav1) or Cav3 and one of the cavin proteins [6, 9–11]. Recent *in vitro* work has shown that plasma membrane caveolae constitute a membrane reservoir that can buffer mechanical stresses such as stretching or osmotic swelling [12]. Moreover, mechanical integrity of vascular and muscle cells is partly dependent on caveolae [13–15]. However, the *in vivo* mechano-protective roles of caveolae have only begun to be explored. Using zebrafish mutants for *cav1*, *cav3*, and *cavin1b*, we show that caveolae are essential for notochord integrity. Upon loss of caveola function, vacuolated cells collapse at discrete positions under the mechanical strain of locomotion. Then, sheath cells invade the inner notochord and differentiate into vacuolated cells, thereby restoring notochord function and allowing normal spine development. Our data further indicate that nucleotides released by dying vacuolated cells promote sheath cell vacuolization and trans-differentiation. This work reveals a novel structural role for caveolae in vertebrates and provides unique insights into the mechanisms that safeguard notochord and spine development.

RESULTS AND DISCUSSION

Caveolin 1 Is a Conserved Vacuolated Cell Plasma Membrane Protein in the Vertebrate Notochord

We previously generated a bacterial artificial chromosome (BAC) transgenic line expressing caveolin 1 (Cav1)-GFP under its own regulatory sequences [16]. Live confocal microscopy of 48 hr post-fertilization (hpf) embryos revealed robust expression in both sheath (marked by *col9a2:mcherry*) and vacuolated cells of the notochord (Figures S1A–S1C). To determine where Cav1-GFP localizes, we isolated vacuolated cells from 48 hpf Cav1-GFP embryos expressing a cytoplasmic mcherry fusion protein or labeled the cell surface with fluorescent wheat germ agglutinin (WGA). Using live confocal microscopy, we observed that Cav1-GFP was confined to the plasma membrane, marked with WGA, often in small punctae, and could not be detected in the vacuole membrane or in intracellular compartments (Figures S1D–S1I). This is consistent with the high concentration of caveolae present at the plasma membrane of notochord vacuolated cells [5] (see also Figure S4). Next, we wanted to determine whether caveolin 1 expression and localization are conserved in mammalian notochord cells. In vertebrates, notochord vacuolated cells can be found in the nucleus pulposus (NP) at the center of intervertebral discs (IVDs) [17]. We obtained pig spines, dissected NPs, and dissociated the tissue to generate isolated notochord cells [18]. Differential interference contrast (DIC) microscopy revealed a striking resemblance in structure and even size between pig NP cells and vacuolated cells isolated from embryonic zebrafish notochords (Figures S1J and S1K). Confocal microscopy of pig NP cells stained for CAV1 showed a dense concentration of punctae on the plasma membrane, labeled with WGA, which may correspond to caveolae (Figures S1L and S1M). In agreement, using electron microscopy (EM), we detected abundant caveolae at the plasma membrane of NP cells (Figure S1J). These data indicate that caveolae are conserved plasma membrane structures in notochord vacuolated cells.

Loss of Caveolae Renders Notochord Vacuolated Cells Prone to Mechanical Disruption during Locomotion

To investigate the function of caveolae in the zebrafish notochord, we generated mutants for the caveolar genes *cav3* and *cavin1b* by genome editing, and used the previously generated *cav1^{pd1104}* allele, which has a mutation that disrupts both *cav1* transcripts [16]. These three genes constitute the only genes essential for caveola formation expressed in the notochord ([5, 6] and J.B. and M.B., unpublished data). The *cav3^{pd1149}* mutant allele was generated using two CRISPRs that remove a 765-bp region between exon 1 and intron 1, resulting in the deletion of 90 bp of coding sequence and a predicted early stop codon after amino acid (aa) 13 (Figures S2A and S2D). Using RT-PCR, we found that *cav1^{pd1104}* is subject to non-sense-mediated decay (Figure S2F). The *cavin1b^{bns110}* allele contains a 7-nt deletion that creates an early stop codon at aa 155, i.e., before the end of the second coiled-coil domain (Figure S2G). This mutation truncates the predicted protein from both *cavin1b* transcripts and causes decay of the long transcript, but does not eliminate the short transcript (Figure S2H).

The single *cav1* and *cav3* zygotic or maternal zygotic (mz) mutants show no gross morphological defects and are adult viable and fertile. Close examination of the notochord revealed no apparent defects in either zygotic or mz mutants (Figure S3A). We then examined *cav1; cav3* double mutants (*cav1, 3^{-/-}* henceforth) and single *cavin1b* mutants and found they present no gross anatomical defects (Figures 1A–1F). However, close examination of zygotic *cav1, 3* and *cavin1b* mutants revealed disruptions of their notochord structure, starting around the time of embryo hatching (between 48 and 72 hpf). By DIC microscopy, vacuolated cells in 72 hpf larvae appeared disrupted in both *cav1, 3* and *cavin1b* mutants (Figures 1A–1F). The penetrance and severity of the notochord lesions are essentially the same for both zygotic mutants ($p > 0.1$, t test) (Figures S3C and S3D). We then used a BODIPY TR methylester dye (MED) to visualize vacuole membranes in live larvae [2] and observed a dramatic collapse of vacuolated cells and the presence of cellular debris in some areas (Figures 1A–1F), which became more extensive and pronounced by 96 hpf (Figures 1G and 1H). We then examined mz mutants and found that although the penetrance and severity of the notochord phenotype are higher at 72 hpf in mz compared to zygotic *cav1, 3* or *cavin1b* mutants (Figures S3B–S3F), the onset still occurs after 48 hpf. Because notochord vacuoles are required for axis elongation [2], we measured body length and found that mz but not zygotic mutants present a small but significant reduction in body length compared to heterozygous larvae at 72 and 120 hpf (Figures S3G–S3I). This difference is most likely due to the later onset of notochord phenotype in zygotic compared to mz mutants. In spite of presenting severe notochord defects, neither *cav1, 3* nor *cavin1b* mutants present spine defects (Figures S3J–S3M). At the ultra-structural level, the plasma membrane of mz *cav1, 3* mutants showed a sharp reduction in caveola formation compared to WT as well as the presence of finger-like invaginations that may correspond to misshapen caveolae (Figures S4A–S4C). The unexpected finding of a few caveolae still present prompted us to explore whether alternative *cav3* transcripts are generated. RT-PCR revealed that in mz *cav1, 3* mutants, but not in heterozygous fish, the *cav3^{pd1149}* transcript is spliced,

generating a predicted alternative start site in the first ATG of the second exon (Figures S2B and S2C). Translation of the mutant transcript would generate a smaller protein missing the N terminus and part of the oligomerization domain but retaining the rest of the protein (Figure S2E). This striking compensatory splicing event may allow mz *cav1, 3* mutants to form the few normal and the dysmorphic caveolae we detected. In mz *cavin1b* mutants, we also observed a sharp reduction in caveola formation compared to WT and the presence of dysmorphic caveolae (Figures S4D–S4H). The small number of caveolae still present suggests that the mutated protein retains some residual activity. Altogether, these data indicate that in our *cav1, 3* and *cavin1b* mutant alleles, caveola formation and function are severely impaired to a similar extent and that the remaining caveolae are insufficient in number and/or are not functional. Because the notochord phenotypes of *cav1, 3* and *cavin1b* mutants are essentially identical, subsequent studies were done using *cavin1b* mutants only.

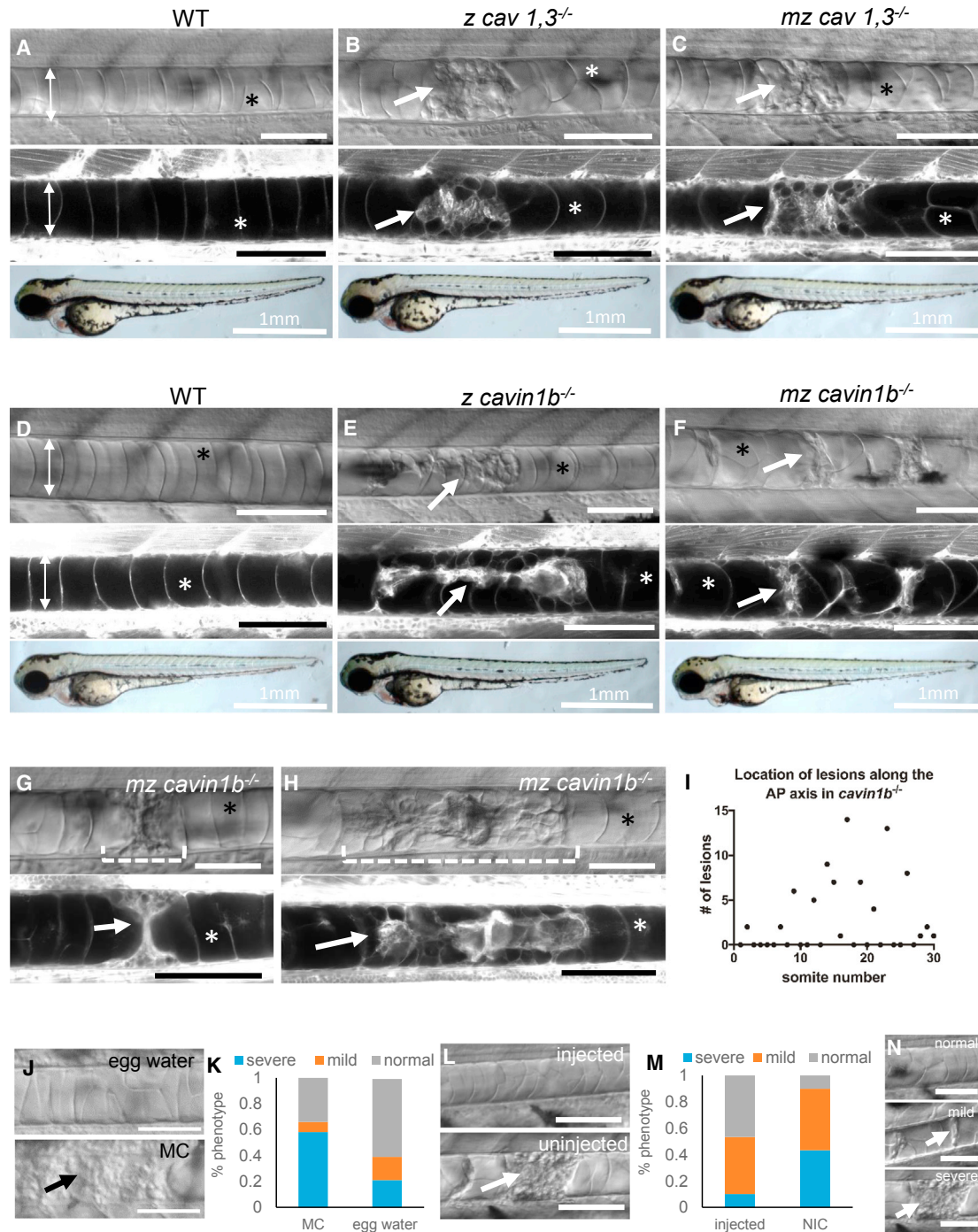
Next, we plotted the location of notochord lesions in 72 hpf zygotic *cavin1b* mutants along the body axis and found that they peaked around somite number 17 (Figure 1I). This point coincides with the region of maximum axial bending during the propulsive stroke of swimming larvae [19].

The spatial distribution of notochord lesions and their onset suggested that notochord lesions are triggered by locomotion. To test this hypothesis, we devised a simple experiment to either enhance or reduce the effect of locomotion. To increase mechanical strain, we de-chorionated 24 hpf mz *cavin1b^{-/-}* embryos and placed them in egg water or in 3% methyl cellulose (MC) to increase the viscosity of the medium as previously shown [14]. To abrogate the effect of locomotion, we injected one-cell-stage mz *cavin1b^{-/-}* embryos with α -bungarotoxin cRNA to paralyze them [20] and incubated them (without removing the chorion) in egg water. Then, at 72 hpf, we used DIC microscopy to score the notochord phenotype into three categories: normal (no lesions), mild (one or more areas with limited vacuole collapse), and severe (one or more areas with extended vacuole collapse and debris) (Figure 1N). Interestingly, incubation in MC significantly increased the number and severity of notochord lesions, whereas α -bungarotoxin injection significantly rescued the notochord phenotype (Figures 1J–1M). De-chorionation reduced the severity of notochord lesions (compare both controls), most likely due to the absence of axial bending inside the chorion and hatching movements.

Together, these data indicate that caveola function is necessary to resist the mechanical load exerted on the notochord by the bending of the axis during swimming strokes.

Collapse of Vacuolated Cells Triggers Sheath Cell Invasion

We next wanted to characterize in better detail the nature and progression of lesions by monitoring both notochord cell types. To this end, we isolated a promoter element from *col9a2* to drive expression of transgenes in sheath cells, and a sequence from the *col8a1a* promoter for vacuolated cells, and established several new sheath and vacuolated cell-specific transgenic lines. In addition, we also used a previously published Gal4 line that drives expression of UAS transgenes in vacuolated cells [1].



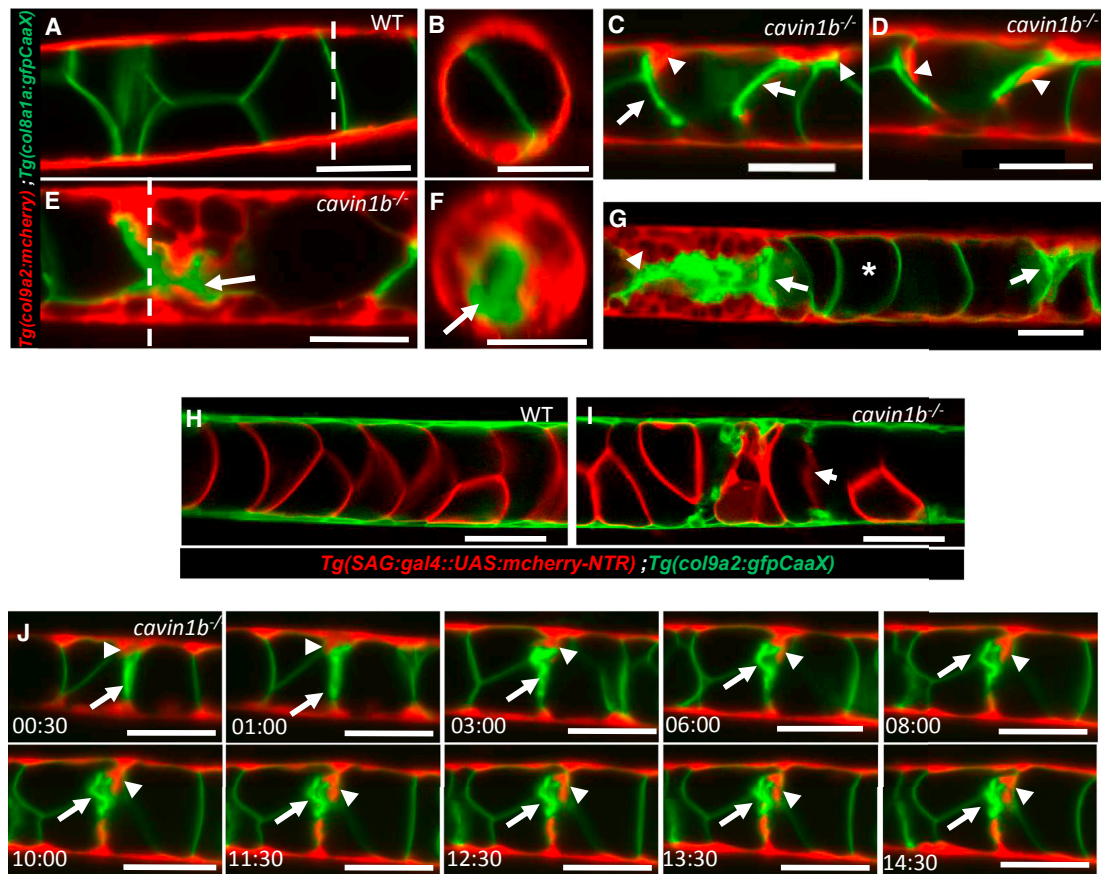


Figure 2. Collapse of Vacuolated Cells Triggers Sheath Cell Invasion

(A and B) Lateral and orthogonal views of a live 72 hpf WT larva expressing *col8a1a:GFPCaaX* in vacuolated cells and *col9a2:mcherry* in sheath cells. The dashed lines in (A) mark the AP level in which the optical cross sections shown in (B) were taken. (C and D) In *cavin1b* mutants with mild lesions, individual sheath cells wedge and invade the inner notochord where vacuolated cells have collapsed. (E and F) Lateral and orthogonal views of a live 72 hpf *cavin1b* mutant with severe lesions showing multiple invading sheath cells. The dashed lines in (E) mark the AP level at which the optical cross sections shown in (F) were taken. (G) Confocal image of a live 72 hpf *cavin1b* mutant with two notochord lesions in close proximity (arrows). The asterisk marks an intact vacuolated cell. (H and I) Confocal images of a live 72 hpf WT and a *cavin1b*^{-/-} mutant expressing *sag:gal4::UAS:mcherry-NTR* in vacuolated cells and *col9a2:GFPCaaX* in sheath cells. Collapsed vacuolated cells lose cytoplasmic contents. (J) Still frames from a 15-hr LSM time-lapse movie showing sheath cells expressing *col9a2:mcherry* invading the inner notochord next to a collapsed vacuolated cell expressing *col8a1a:GFPCaaX*.

Arrows point to a collapsed vacuolated cell; arrowheads indicate an invading sheath cell. Scale bars, 50 μ m. Error bars are SD. See also [Figures S2–S4](#) and [Movies S1](#) and [S2](#).

We first examined *cavin1b* mutants and WT siblings expressing *col9a2:mcherry* and *col8a1a:GFPCaaX* to label the cytoplasm of sheath cells and the plasma membrane of vacuolated cells, respectively. Using light sheet microscopy (LSM) [21], we found that notochord lesions judged to be mild by DIC microscopy correspond to collapsed vacuolated cells (Figure 2C). Unexpectedly, we also found sheath cells inside the notochord that were tightly associated with the collapsed vacuolated cells (Figure 2D). In contrast, in WT siblings, we never observed a sheath cell within the notochord core (Figures 2A and 2H). LSM imaging of *cavin1b* mutants with severe lesions revealed extended areas with vacuolated cell collapse with sheath cells surrounding them (Figures 2E and 2F). However, these clusters of collapsed cells did not seem to affect nearby areas, as we could find intact vacuolated cells without ectopic sheath cells between two close le-

sions (Figure 2G). Importantly, in all cases, the notochord sheath appeared intact, with a continuous and seemingly normal epithelium.

Next, we examined 72 hpf *cavin1b*^{-/-} larvae expressing *col9a2:GFPCaaX* to label the plasma membrane of sheath cells and *SAG214:Gal4; UAS:mcherry-NTR* to label the cytoplasm of vacuolated cells. Live imaging revealed sheath cells within the notochord core and diffuse or absent mcherry signal in collapsed vacuolated cells, suggesting that the plasma membrane had ruptured in those cells (Figure 2I). Because movement triggers vacuolated cell collapse, we were unfortunately unable to film a collapsing cell. However, direct observation of fish before and after vigorous movement suggests the collapse process is rapid.

In notochord areas with vacuolated cell collapse, we readily found sheath cells wedging toward the remnants of

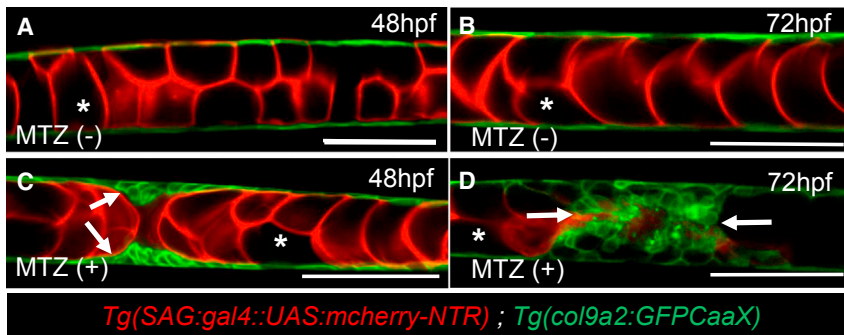
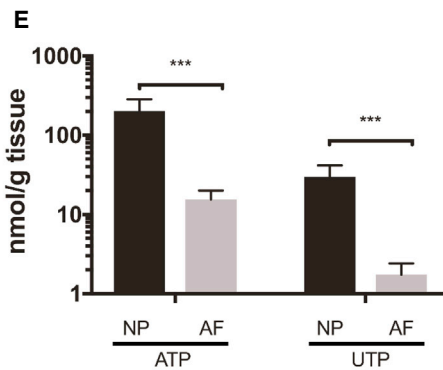


Figure 3. Release of Vacuolated Cell Contents Triggers Sheath Cell Invasion

(A and B) Confocal images of live WT embryos expressing *sag:gal4::UAS:mcherry-NTR* in vacuolated cells and *col9a2:GFP-CaaX* in sheath cells.

(C and D) In embryos treated with 1.5 mM metronidazole (MTZ), sheath cells invade areas of vacuolated cell death. Arrows point to invading sheath cells; asterisks mark intact vacuolated cells.

(E) LC-MS quantitation of ATP and UTP levels in nucleus pulposus (NP) and annulus fibrosus (AF) tissue isolated from 6-month-old pig spines. $n = 12$ for NP and 4 for AF. $***p < 0.001$, Student's *t* test. The scale bars represent 100 μ m. Error bars are SD. See also [Figures S3](#) and [S4](#).



vacuolated cells ([Figure 2C](#)), suggesting that cells delaminate from the sheath epithelium into the inner notochord in *cavin1b* mutants. To test this hypothesis, we identified 72 hpf *cavin1b* mutants expressing *col9a2:mcherry* and *col8a1a:GFP-CaaX* with mild notochord lesions and imaged them using LSM. Under these conditions, the larvae are immobilized and no new lesions are generated. We observed single sheath cells within the sheath epithelium wedging toward a collapsed vacuolated cell, then delaminating and moving slowly over the collapsed cell in a span of 15 hr ([Figure 2J](#); [Movies S1](#) and [S2](#)).

Collectively, these data indicate that upon loss of caveolae, vacuolated cells collapse, most likely due to rupture of the plasma membrane, leading to the ingress of sheath cells through a slow delamination and migration process.

Release of Vacuolated Cell Contents Triggers Sheath Cell Invasion

We next investigated whether sheath cell invasion is triggered specifically by the loss of caveolae or by the death of vacuolated cells. To this end, we took 24 hpf WT embryos expressing nitroreductase (NTR) in vacuolated cells and *col9a2:GFP-CaaX* in sheath cells and treated them with metronidazole (mtz). NTR converts mtz into a toxic compound that kills the expressing, but not neighboring, cells [[22](#)]. The mtz treatment we used (1.5 mM for 24 hr) typically kills only some of the NTR-expressing notochord cells. At 48 hpf in mtz-treated, but not control, animals, we observed clusters of sheath cells wedging toward the notochord core ([Figure 3C](#)). One day later, the same region was devoid of vacuolated cells and filled with sheath cells ([Figure 3D](#)). These data indicate that disruption of vacuolated cells triggers sheath cell invasion.

We then hypothesized that the release of vacuolated cell contents promotes sheath cell invasion. To identify candidate molecules enriched in vacuolated cells, we performed a metabolomics analysis [[23](#)] of pig NP, which is largely composed of vacuolated cells [[18](#)], and the surrounding annulus fibrosus (AF) tissue. Using liquid chromatography-mass spectrometry (LC-MS), we analyzed a set of 200 small molecules and found among the most highly enriched compounds in NP versus AF tissue several nucleotides, including UTP, UDP, and ATP (not shown). We then performed quantitative LC-MS [[23](#)] for UTP and ATP and found that both were significantly enriched in NP compared to AF ([Figure 3E](#)). Interestingly, nucleotide release has been shown to promote cell migration in zebrafish [[24](#)] and mammals [[25](#), [26](#)]. Moreover, UTP has been found accumulating within lysosomes [[27](#), [28](#)], and we showed previously that notochord vacuoles are lysosome-related organelles [[2](#)]. Together, these data show that vacuolated cell death releases NTPs, and most likely also other signals, including mechanical stimuli, that may promote sheath cell invasion. The short half-life of extracellular NTPs [[29](#)] may help explain why we always found invading sheath cells in close proximity to collapsed vacuolated cells.

Invading Sheath Cells Differentiate into Vacuolated Cells

We noticed that the invading sheath cells enlarge in size and develop an internal compartment free of cytoplasmic mcherry (see [Figures 2E](#), [2G](#), and [S4G](#)), suggesting that they may form a vacuole upon exposure to vacuolated cell contents. To test this possibility, we imaged 72 hpf *rcn3:GFP-Rab32a; col9a2:mcherry* larvae and found in *cavin1b* mutants with severe notochord lesions a dramatic upregulation of *rcn3:GFP-Rab32a* in sheath cells next to regions of vacuolated cell collapse ([Figures 4A](#) and [4B](#)). We also observed in sheath cells GFP-Rab32a clearly lining the newly formed vacuoles ([Figures 4C](#) and [4D](#)). Next, we tested whether vacuolization of invading sheath cells is triggered by extracellular NTPs. Because after 48 hpf the notochord sheath is highly impermeable to many compounds [[2](#)], we dissociated notochords with or without the addition of the purinergic receptor inhibitors suramin (1 mM) and AR-C 118925XX

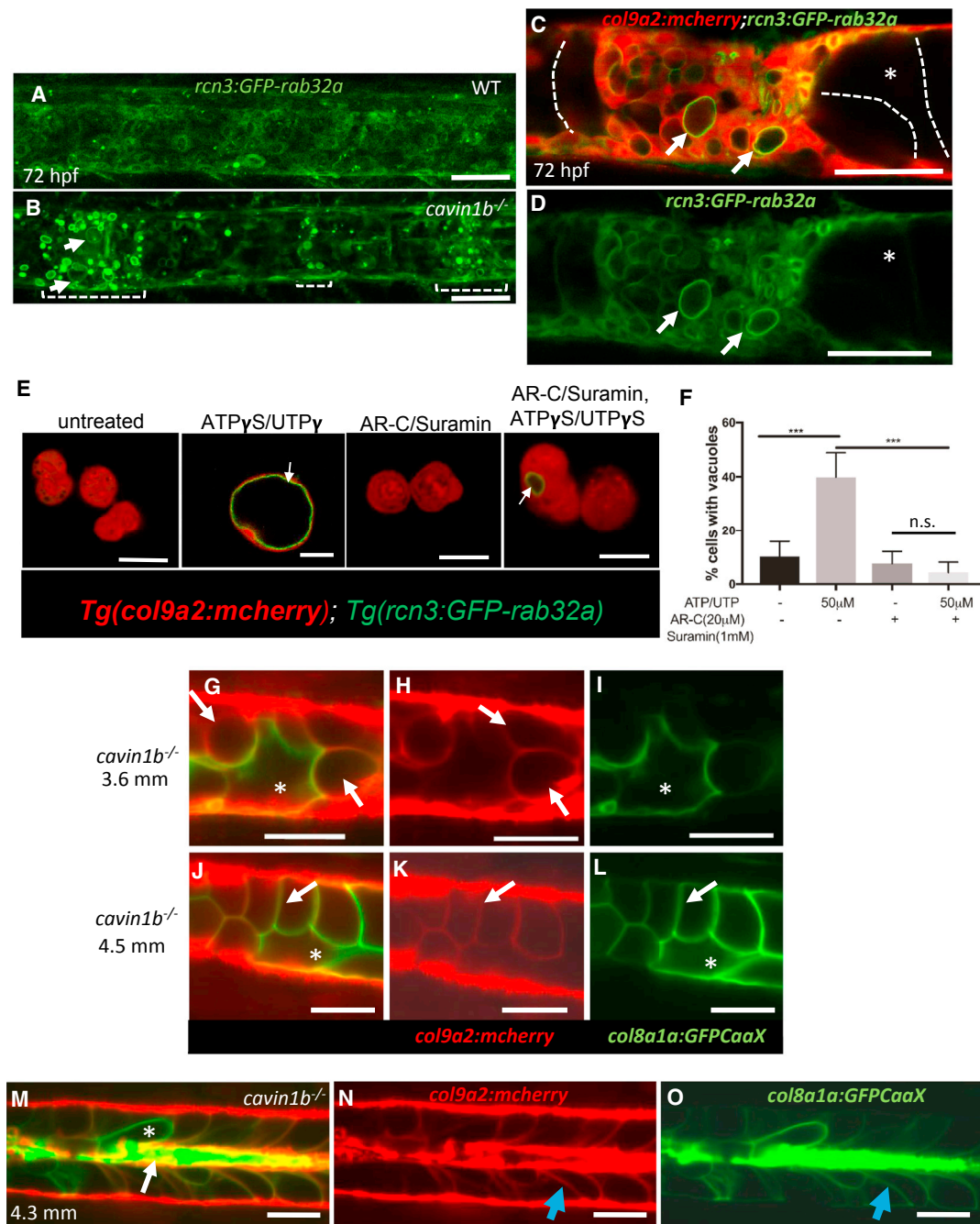


Figure 4. Invading Sheath Cells Differentiate into Vacuolated Cells

(A and B) Projections of confocal stacks of 72 hpf WT and *cavin1b*^{-/-} larvae expressing *rcn3:GFP-rab32a* and *col9a2:mcherry*. Brackets mark areas of vacuolated cell collapse and sheath invasion; arrows point to new vacuoles in sheath cells.

(C and D) Following invasion, sheath cell vacuoles (arrows) enlarge. Intact primary vacuolated cells are traced with dashed lines. The asterisks mark an intact vacuolated cell.

(E) Confocal images of live sheath cells obtained from 48 hpf embryos expressing *col9a2:mcherry* and *rcn3:GFP-rab32a*. Cells were treated with suramin and AR-C 118925XX (AR-C) or ATP_γS/UTP_γS or left untreated for 2 hr. Arrows point to newly formed vacuoles.

(F) Quantitation using one-way ANOVA followed by multiple comparisons using Tukey's test, ***p < 0.001; n.s., not significant; n = 3 experiments.

(G–O) LSM imaging of *cavin1b* mutants expressing *col8a1a:GFPCaaX* and *col9a2:mcherry*.

(G–I) 3.6-mm fish. Arrows point to vacuolated sheath cells; asterisks mark a primary vacuolated cell.

(J–L) 4.5-mm *cavin1b*^{-/-} fish showing new vacuolated cells that retained *col9a2:mcherry* expression (arrows) next to a primary vacuolated cell (asterisks).

(M–O) 4.3-mm *cavin1b*^{-/-} fish with remnants of primary vacuolated cells (arrow), a primary vacuolated cell (asterisk), and newly differentiated vacuolated cells (blue arrows).

Scale bars, 50 μm. Error bars are SD. See also [Figures S3](#) and [S4](#).

(AR-C) (20 μ M) [30] to block the action of NTPs released during the procedure. Then, we plated the dissociated tissues on laminin-coated plates and treated them with a cocktail of hydrolysis-resistant ATP and UTP analogs (ATP γ S and UTP γ S) \pm AR-C and suramin. Interestingly, upon treatment with ATP γ S/UTP γ S for 2 hr, we found a sharp and significant increase in the fraction of cells forming vacuoles lined by GFP-Rab32a [2], which was abrogated by the inhibitors (Figure 4C). These data indicate that NTPs released from collapsed vacuolated cells act on sheath cells to promote vacuolization.

Next, we imaged *cavin1b* mutants expressing *col9a2:mcherry* and *col8a1a:GFPcax* at the 3.6-mm stage [31] and found that the internalized sheath cells continue to enlarge, filling all the space created by the collapse of vacuolated cells (Figures 4G–4I). Until the 3.6-mm stage, sheath cells retain the sheath marker (*col9a2*) and do not express vacuolated cell markers (i.e., *col8a1a*, *cyb5r2*). However, at around 4.25 mm, we could detect expression of *col8a1a:GFPcax* in cells that retained *col9a2:mcherry*, indicating that they have switched to the mature vacuolated cell profile (Figures 4J–4L). We also observed that remnants of collapsed vacuolated cells persisted at the center of the notochord for several days (Figures 4M–4O), possibly leading to the formation of a scar. Together, these data reveal that the internalized sheath cells differentiate into new vacuolated cells in response to signals from the dying vacuolated cells.

In this study, we demonstrate a mechano-protective role for caveolae in the zebrafish notochord. Loss of caveolar function results in a dramatic collapse of vacuolated cells due to the mechanical strain of locomotion. Strikingly, we found that vacuolated cell collapse leads to sheath cell invasion and trans-differentiation into new vacuolated cells, thereby replacing the collapsed cells and supporting normal spine development. Biochemical assays and experimental manipulations indicate that the release of NTPs from collapsed vacuolated cells triggers sheath cell vacuolization and possibly also invasion. Our data also suggest that chordomas, rare and aggressive notochord cell tumors [32], originate from the invasion of sheath cells into other tissues. Altogether, this work demonstrates a critical role for caveolae in maintaining the structural integrity of the notochord and reveals a novel protective response that safeguards spine development.

STAR★METHODS

Detailed methods are provided in the online version of this paper and include the following:

- KEY RESOURCES TABLE
- CONTACT FOR REAGENT AND RESOURCE SHARING
- EXPERIMENTAL MODEL AND SUBJECT DETAILS
 - Fish stocks
- METHOD DETAILS
 - Genome editing
 - Locomotion dependency of notochord lesions
 - Calcein staining and skeletal preparations
 - Microscopy
 - Dissociated notochord assay
 - Metabolomics
 - Electron Microscopy
- QUANTIFICATION AND STATISTICAL ANALYSIS

SUPPLEMENTAL INFORMATION

Supplemental Information includes four figures and two movies and can be found with this article online at <http://dx.doi.org/10.1016/j.cub.2017.05.035>.

AUTHOR CONTRIBUTIONS

Conceptualization, M.B.; Methodology, M.B., D.Y.R.S., J.B., J.G., D.S.L., X.L., and J.W.L.; Validation, J.G., J.B., D.S.L., and J.N.; Formal Analysis, M.B., J.G., X.L., and D.S.L.; Investigation, J.G., J.B., B.N., S.W., X.L., D.S.L., S.E.M., J.N., and M.B.; Writing – Original Draft, M.B.; Writing – Review & Editing, M.B., D.Y.R.S., and J.W.L.; Visualization, J.B. and M.B.; Supervision, M.B., D.Y.R.S., and J.W.L.; Project Administration, M.B. and J.B.; Funding Acquisition, M.B. and D.Y.R.S.

ACKNOWLEDGMENTS

We thank the Duke zebrafish facility for fish care, the Duke light microscopy facility for help with image acquisition, Janice Williams for EM, Jun Chen for help in obtaining IVD tissue, Stefano di Talia for the use of his confocal microscope, and Cagla Eroglu and Ken Poss for critical reading of this manuscript. This work was supported by NIH grants AR065439 (M.B.), AR065439-04S1 (J.G.), T32DK007568-26 (D.S.L.), and CA193256 (J.W.L.), a Capes-Humboldt fellowship (B.N.), and the Max Planck Society (D.Y.R.S.). The research of M.B. was supported in part by a Faculty Scholar grant from the Howard Hughes Medical Institute.

Received: February 12, 2017

Revised: April 7, 2017

Accepted: May 9, 2017

Published: June 22, 2017

REFERENCES

1. Yamamoto, M., Morita, R., Mizoguchi, T., Matsuo, H., Isoda, M., Ishitani, T., Chitnis, A.B., Matsumoto, K., Crump, J.G., Hozumi, K., et al. (2010). Mib-Jag1-Notch signalling regulates patterning and structural roles of the notochord by controlling cell-fate decisions. *Development* **137**, 2527–2537.
2. Ellis, K., Bagwell, J., and Bagnat, M. (2013). Notochord vacuoles are lysosome-related organelles that function in axis and spine morphogenesis. *J. Cell Biol.* **200**, 667–679.
3. Ellis, K., Hoffman, B.D., and Bagnat, M. (2013). The vacuole within: how cellular organization dictates notochord function. *BioArchitecture* **3**, 64–68.
4. Adams, D.S., Keller, R., and Koehl, M.A. (1990). The mechanics of notochord elongation, straightening and stiffening in the embryo of *Xenopus laevis*. *Development* **110**, 115–130.
5. Nixon, S.J., Carter, A., Wegner, J., Ferguson, C., Floetenmeyer, M., Riches, J., Key, B., Westerfield, M., and Parton, R.G. (2007). Caveolin-1 is required for lateral line neuromast and notochord development. *J. Cell Sci.* **120**, 2151–2161.
6. Hill, M.M., Bastiani, M., Luetterforst, R., Kirkham, M., Kirkham, A., Nixon, S.J., Walsler, P., Abankwa, D., Oorschot, V.M., Martin, S., et al. (2008). PTRF-Cavin, a conserved cytoplasmic protein required for caveola formation and function. *Cell* **132**, 113–124.
7. Stoerber, M., Schellenberger, P., Siebert, C.A., Leyrat, C., Helenius, A., and Grünwald, K. (2016). Model for the architecture of caveolae based on a flexible, net-like assembly of Cavin1 and Caveolin discs. *Proc. Natl. Acad. Sci. USA* **113**, E8069–E8078.
8. Parton, R.G., and del Pozo, M.A. (2013). Caveolae as plasma membrane sensors, protectors and organizers. *Nat. Rev. Mol. Cell Biol.* **14**, 98–112.
9. Ludwig, A., Howard, G., Mendoza-Topaz, C., Deerinck, T., Mackey, M., Sandin, S., Ellisman, M.H., and Nichols, B.J. (2013). Molecular composition and ultrastructure of the caveolar coat complex. *PLoS Biol.* **11**, e1001640.

10. Ariotti, N., and Parton, R.G. (2013). SnapShot: caveolae, caveolins, and cavins. *Cell* *154*, 704–704.e1.
11. Shvets, E., Ludwig, A., and Nichols, B.J. (2014). News from the caves: update on the structure and function of caveolae. *Curr. Opin. Cell Biol.* *29*, 99–106.
12. Sinha, B., Köster, D., Ruez, R., Gonnord, P., Bastiani, M., Abankwa, D., Stan, R.V., Butler-Browne, G., Védie, B., Johannes, L., et al. (2011). Cells respond to mechanical stress by rapid disassembly of caveolae. *Cell* *144*, 402–413.
13. Cheng, J.P., Mendoza-Topaz, C., Howard, G., Chadwick, J., Shvets, E., Cowburn, A.S., Dunmore, B.J., Crosby, A., Morrell, N.W., and Nichols, B.J. (2015). Caveolae protect endothelial cells from membrane rupture during increased cardiac output. *J. Cell Biol.* *211*, 53–61.
14. Lo, H.P., Nixon, S.J., Hall, T.E., Cowling, B.S., Ferguson, C., Morgan, G.P., Schieber, N.L., Fernandez-Rojo, M.A., Bastiani, M., Floetenmeyer, M., et al. (2015). The caveolin-cavin system plays a conserved and critical role in mechanoprotection of skeletal muscle. *J. Cell Biol.* *210*, 833–849.
15. Lo, H.P., Hall, T.E., and Parton, R.G. (2016). Mechanoprotection by skeletal muscle caveolae. *BioArchitecture* *6*, 22–27.
16. Cao, J., Navis, A., Cox, B.D., Dickson, A.L., Gemberling, M., Karra, R., Bagnat, M., and Poss, K.D. (2016). Single epicardial cell transcriptome sequencing identifies caveolin 1 as an essential factor in zebrafish heart regeneration. *Development* *143*, 232–243.
17. Lawson, L., and Harfe, B.D. (2015). Notochord to nucleus pulposus transition. *Curr. Osteoporos. Rep.* *13*, 336–341.
18. Chen, J., Yan, W., and Setton, L.A. (2006). Molecular phenotypes of notochordal cells purified from immature nucleus pulposus. *Eur. Spine J.* *15 (Suppl 3)*, S303–S311.
19. Müller, U.K., van den Boogaart, J.G., and van Leeuwen, J.L. (2008). Flow patterns of larval fish: undulatory swimming in the intermediate flow regime. *J. Exp. Biol.* *211*, 196–205.
20. Swinburne, I.A., Mosaliganti, K.R., Green, A.A., and Megason, S.G. (2015). Improved long-term imaging of embryos with genetically encoded α -bungarotoxin. *PLoS ONE* *10*, e0134005.
21. Huisken, J., Swoger, J., Del Bene, F., Wittbrodt, J., and Stelzer, E.H. (2004). Optical sectioning deep inside live embryos by selective plane illumination microscopy. *Science* *305*, 1007–1009.
22. Curado, S., Stainier, D.Y., and Anderson, R.M. (2008). Nitroreductase-mediated cell/tissue ablation in zebrafish: a spatially and temporally controlled ablation method with applications in developmental and regeneration studies. *Nat. Protoc.* *3*, 948–954.
23. Liu, X., Ser, Z., and Locasale, J.W. (2014). Development and quantitative evaluation of a high-resolution metabolomics technology. *Anal. Chem.* *86*, 2175–2184.
24. Gault, W.J., Enyedi, B., and Niethammer, P. (2014). Osmotic surveillance mediates rapid wound closure through nucleotide release. *J. Cell Biol.* *207*, 767–782.
25. Schneider, G., Glaser, T., Lameu, C., Abdelbaset-Ismael, A., Sellers, Z.P., Moniuszko, M., Ulrich, H., and Ratajczak, M.Z. (2015). Extracellular nucleotides as novel, underappreciated pro-metastatic factors that stimulate purinergic signaling in human lung cancer cells. *Mol. Cancer* *14*, 201.
26. Corriden, R., and Insel, P.A. (2012). New insights regarding the regulation of chemotaxis by nucleotides, adenosine, and their receptors. *Purinergic Signal.* *8*, 587–598.
27. Lazarowski, E.R. (2012). Vesicular and conductive mechanisms of nucleotide release. *Purinergic Signal.* *8*, 359–373.
28. Cao, Q., Zhao, K., Zhong, X.Z., Zou, Y., Yu, H., Huang, P., Xu, T.L., and Dong, X.P. (2014). SLC17A9 protein functions as a lysosomal ATP transporter and regulates cell viability. *J. Biol. Chem.* *289*, 23189–23199.
29. Zimmermann, H., Zebisch, M., and Sträter, N. (2012). Cellular function and molecular structure of ecto-nucleotidases. *Purinergic Signal.* *8*, 437–502.
30. von Kügelgen, I., and Hoffmann, K. (2016). Pharmacology and structure of P2Y receptors. *Neuropharmacology* *104*, 50–61.
31. Parichy, D.M., Elizondo, M.R., Mills, M.G., Gordon, T.N., and Engeszer, R.E. (2009). Normal table of postembryonic zebrafish development: staging by externally visible anatomy of the living fish. *Dev. Dyn.* *238*, 2975–3015.
32. Sun, X., Hornicek, F., and Schwab, J.H. (2015). Chordoma: an update on the pathophysiology and molecular mechanisms. *Curr. Rev. Musculoskelet. Med.* *8*, 344–352.
33. Westerfield, M. (2000). *The Zebrafish Book: A Guide for the Laboratory Use of Zebrafish (Danio rerio)* (University of Oregon Press).
34. Bagnat, M., Navis, A., Herbstreith, S., Brand-Arzamendi, K., Curado, S., Gabriel, S., Mostov, K., Huisken, J., and Stainier, D.Y. (2010). Cse1l is a negative regulator of CFTR-dependent fluid secretion. *Curr. Biol.* *20*, 1840–1845.

STAR★METHODS

KEY RESOURCES TABLE

REAGENT or RESOURCE	SOURCE	IDENTIFIER
Antibodies		
Mouse monoclonal Anti-Caveolin 1	BD Biosciences	Cat#610406; RRID: AB_397788
Wheat Germ Agglutinin, Alexa Fluor 594 Conjugate	ThermoFisher	Cat#W11262
Biological Samples		
Porcine intervertebral disc tissue	Duke University Department of Orthopaedics	N/A
Chemicals, Peptides, and Recombinant Proteins		
Suramin	Sigma-Aldrich	Cat# S2671
AR-C 118925XX	Tocris	Cat# 4890
LC-MS Uridine-13C9,15N2 5'-triphosphate sodium salt	Sigma-Aldrich	Cat#645672
LC-MS Adenosine-13C10,15N5 5'-monophosphate sodium salt	Sigma-Aldrich	Cat#650676
Sodium cacodylate	Electron Microscopy Sciences	Cat#11650
Glutaraldehyde	Electron Microscopy Sciences	Cat#16320
Paraformaldehyde	Fisher	Cat#AC416780250
Leibovitz's L-15 media	ThermoFisher	Cat#21083-027
ATP γ S trisodium salt	Abcam	Cat#ab138911
UTP γ S trisodium salt	Tocris	Cat#3279
Trypsin-EDTA	ThermoFisher	Cat#25200056
Collagenase	Sigma-Aldrich	Cat#C2674
Osmium Tetroxide	Electron Microscopy Sciences	Cat#19134
Calcein	Sigma-Aldrich	Cat#0875
Alizarin red	Sigma-Aldrich	Cat#A5533
Experimental Models: Organisms/Strains		
Zebrafish: Tg(col9a2:mcherry)pd1150	This work	N/A
Zebrafish: Tg(col8a1a:GFPCaaX)pd1152	This work	N/A
Zebrafish: Tg(rcn3:GFPrab32a)pd1153	This work	N/A
Zebrafish: Tg(col9a2:GFPCaaX)pd1151	This work	N/A
Zebrafish: cavin1bbns110	This work	N/A
Zebrafish: cav3pd1149	This work	N/A
Zebrafish: cav1pd1104	[16]	N/A
Zebrafish: Tg(sag:gal4::UAS:mcherry-NTR)	[2]	N/A
Zebrafish: Tg(cav1-spGFP)pd1096	[16]	N/A
Oligonucleotides		
Guide RNA: cavin1b- 5'CGTGAACGTCAAG TCGGTGCGGG3'	This work	N/A
Guide RNA: cav3-1- 5'CTACTTCTAGTT GTAGG 3'	This work	N/A
Guide RNA: cav3-2- 5'GGACCAGTACAA CACTAACG 3'	This work	N/A
Recombinant DNA		
Pmtb-t7-alpha-bungarotoxin	[20]	Addgene plasmid#69542
Software and Algorithms		
Graphpad	GraphPad Software, La Jolla California USA	https://www.graphpad.com/scientific-software/prism/ ; RRID: SCR_002798

CONTACT FOR REAGENT AND RESOURCE SHARING

Further information and requests for resources and reagents should be directed to and will be fulfilled by the Lead Contact Michel Bagnat (m.bagnat@cellbio.duke.edu).

EXPERIMENTAL MODEL AND SUBJECT DETAILS

Animal experiments were approved by the Duke Institutional Animal Care and Use Committee (IACUC).

Fish stocks

Zebrafish (*Danio rerio*) stocks were maintained at 28°C and bred as previously described [33]. Zebrafish were raised in a circulating aquarium in tanks housing 1-10 fish/L. Zebrafish stocks were healthy and of normal immune status, not involved in previous procedures, and were drug test naive. Genotype of zebrafish are specified in each figure legend. Male and female breeders from 3-9 months of age were used to generate fish for all experiments. 3-5dpf zebrafish larvae from the Ekkwill (EK) background were used in this study. Strains generated for this study: Tg(col9a2:mcherry)pd1150, Tg(col8a1a:GFPCaaX)pd1152, Tg(rcn3:GFPab32a)pd1153, Tg(col9a2:GFPCaaX)pd1151, *cavin1bbns110*, *cav3pd1149*. Previously published strains: *cav1pd1104* [16], Tg(sag:gal4::UAS:mcherry-NTR) [2], Tg(*cav1-spGFP*)pd1096 [16].

METHOD DETAILS

Genome editing

Mutant lines were generated using CRISPR/Cas9. *cav3* mutants were generated using CRISPRs targeting exon 1 and intron 1. *cavin1b* mutants were generated a CRISPR that targets exon 1. Guide RNAs: *cavin1b*- 5'CGTGAACGTCAAGTCGGTGCGGG3', *cav3-1*- 5'CTACTTCTAGTTGTAGG 3', *cav3-2*- 5'GGACCAGTACAACACTAACG 3'. Zebrafish embryos were injected at the one-cell stage with 100pg total of CRISPR RNA. Genotyping for *cav3* was performed using primers: forward, TCTCCTATCGGA CACTTCTGC; reverse, TGTCTGTTTGTGACCTTCAA. Genotyping for *cavin1b* was performed using primers: forward, CACAGC CAACACCGTCAATA; reverse, CAGCCTGTTTCTCCAGGTTTC.

Locomotion dependency of notochord lesions

Methyl cellulose treatment: 24hpf *mz cavin 1b^{-/-}* embryos were de-chorionated and placed in 3% methyl cellulose. Control animals were incubated in egg water. At 72hpf, larvae were evaluated for notochord lesions as indicated in the manuscript using a Nikon SMZ800 microscope. This experiment was performed 3 times with an n = 30 animals for each condition per experiment.

α -bungarotoxin injection: One-cell stage *mz cavin 1b^{-/-}* embryos were injected with α -bungarotoxin cRNA (1ng/nL). Control animals were not injected. Injected and non-injected controls were left in their chorions. At 72hpf, larvae were evaluated for notochord lesions as indicated in the manuscript. This experiment was performed 3 times with an n = 30 animals for each condition per experiment.

Calcein staining and skeletal preparations

Larvae were stained with calcein (Sigma-Aldrich) for 15-30 min and then live imaged on a AX10 Zoom V116 Zeiss microscope equipped with a Plan neofluar Z 1x objective. Zebrafish between 21-30dpf were eviscerated and fixed in 4% PFA. They were then stained with alizarin red as previously described [2], and treated with 1% KOH to clear tissue from the bone. Once the skeleton was clear of tissue, the spine was imaged as indicated above.

Microscopy

Whole-mount live imaging, and fixed section imaging were performed on a confocal microscope (SP5; Leica) with 10 × /0.40 HC PL APO air objective and 20 × /0.70 HC PL APO oil objective objective and Application Suite software (Leica). Dissected notochord cells were imaged using a 710 inverted confocal microscope (Carl Zeiss) with 63 × /1.40 Oil Plan-Apochromat objective (Carl Zeiss) and Zen software. Pig vacuolated cell were imaged on an Axio Imager.M1 microscope with 10 × /0.3 EC Plan-NeoFluar objective and 20 × /0.8 Plan-Apochromat objective, an AxioCamMRm camera, and AxioVision software (all from Carl Zeiss). Body length measurements were done on a Setero Discovery.V20 microscope with 1.0 × Achromat S FWD 63 mm objective, an AxioCamHRc camera, and AxioVision software (all from Carl Zeiss). Light sheet microscopy fish were mounted in low melt agarose and imaged using using a Lightsheet Z.1 detection optics 20x/1.0 (water immersion) (Carl Zeiss). Where necessary, images were minimally post-processed in ImageJ software (National Institutes of Health) for overall brightness and contrast or to realign channels to correct for drift that occurs during live imaging.

Dissociated notochord assay

Notochord cells were obtained from various transgenic lines as indicated following previously published methods [2], with minor modifications. Whole larval zebrafish were placed in a solution containing Trypsin-EDTA and 1% collagenase. The fish were kept at 28°C on a shaker to dissociate tissue surrounding the notochord. Individual vacuolated cells were then isolated from

this preparation. As indicated, some preparations included 1mM suramin (Sigma-Aldrich), 20 μ M AR-C 118925XX (Tocris), and/or 50 μ M ATP- γ -S, UTP- γ -S (Tocris). Then cells were plated in L15 medium (GIBCO) in laminin-coated glass plates and incubated for 2 hr in presence of various chemicals as indicated. Cells were then imaged using a 710 inverted confocal microscope (Carl Zeiss). The experiment was repeated 3 times.

Metabolomics

Nucleus pulposus and annulus fibrosus cells were extracted from the intervertebral discs of 6 month old pigs. Once the material was collected with tweezers it was placed in 1.5mL tubes and immediately placed in liquid nitrogen. Once frozen, the tissue was pulverized into a powder that was then processed and analyzed for metabolomic analysis as previously described [23].

Mass Spectrometry: The QE-MS is equipped with a HESI probe, and the relevant parameters are as listed: heater temperature, 120°C; sheath gas, 30; auxiliary gas, 10; sweep gas, 3; spray voltage, 3.6 kV for the positive mode and 2.5 kV for the negative mode. Capillary temperature was set at 320°C, and S-lens was 55. A full scan range from 60 to 900 (m/z) was used. The resolution was set at 70000. The maximum injection time (max IT) was 200 ms with typical injection times around 50 ms. These settings resulted in a duty cycle of around 550 ms to carry out scans in both the positive and negative modes. Automated gain control (AGC) was targeted at 3 \times 10⁶ ions. For MS/MS, the isolation width of the precursor was set at 2.5, HCD collision energy was 35%, and max IT is 100 ms. The resolution and AGC were 35000 and 200000, respectively. Full scan with resolution at 35000 and IT of 100 ms) was run together with MS/MS. Customized mass calibration was performed before any sample analysis.

High-Performance Liquid Chromatography: The HPLC (Ultimate 3000 UHPLC) is coupled to QE-MS (Thermo Scientific) for metabolite separation and detection. An Xbridge amide column (100 \AA \times 2.1 mm i.d., 3.5 μ m; Waters) is employed for compound separation at room temperature. The mobile phase A is 20 mM ammonium acetate and 15 mM ammonium hydroxide in water with 3% acetonitrile, pH 9.0, and mobile phase B is acetonitrile. The linear gradient used is as follows: 0 min, 85% B; 1.5 min, 85% B, 5.5 min, 35% B; 10 min, 35% B, 10.5 min, 35% B, 14.5 min, 35% B, 15 min, 85% B, and 20 min, 85% B. The flow rate was 0.15 mL/min from 0 to 10 min and 15 to 20 min and 0.3 mL/min from 10.5 to 14.5 min.

For quantitative LC-MS Uridine-13C₉,15N₂ 5'-triphosphate sodium salt and Adenosine-13C₁₀,15N₅ 5'-triphosphate sodium salt (Sigma-Aldrich) were used as standards.

Electron Microscopy

NP tissue was fixed overnight at 4°C in 0.1M sodium cacodylate, 2% para-formaldehyde (PFA), and 2.5% glutaraldehyde (GA). Zebrafish larvae were fixed in 0.1M sodium cacodylate, and 2.5% GA. Specimen preparation and staining was done as previously described [34]. Briefly, after fixation, samples were stained with osmium tetroxide and uranyl acetate. Then samples were then dehydrated in ethanol solutions of increasing concentration and embedded in resin blocks overnight and then embedded and cured in a 60 degree oven for 48 hr. Then thin sections were cut and post-stained with lead citrate and uranyl acetate and placed on copper grids for imaging. Caveolae formation was quantified by counting the number of omega shaped structures present per 1 μ m of plasma membrane.

QUANTIFICATION AND STATISTICAL ANALYSIS

GraphPad Prism version 7.0c for Mac, GraphPad Software, La Jolla California USA, <http://www.graphpad.com> was used to plot and analyze data. Specific statistical data (n values) can be found within the figure legends. The n values listed in each figure legend represent the number of animals or the number of experimental replicates. In Figure 1, n represents the number of animals. A Fisher's exact test was used here to compare the nominal variables. In Figure 3, n represents the number for samples. In Figure 4, n represents the number of experimental replicates. One-way ANOVA followed by Tukey's multiple comparisons test was performed for this dataset. For body length experiments in Figure S3, n represents the number of animals. One-way ANOVA followed by Tukey's multiple comparisons test was performed on this dataset.